<div align="right">

4

</div>

Turbulent Flow Simulation over a Bluff Body

In this chapter, a set of numerical simulations using LBM are presented to test and compare the of different velocity distribution models of LBM and boundary conditions on the turbulent flow pattern. Hence, two studies have been performed on the benchmark case of turbulent flow past over a bluff body. First, how the different discrete velocity models of LBM affect the turbulent flow behavior past over a bluff body is explored. Second, the changes observed on the flow pattern on implementing different boundary conditions on the bluff body to achieve a no-slip condition are demonstrated.

The present work aims to address the aforementioned problems. A detailed discussion on the simulation methodology is presented in the next section. Our key contributions for this chapter are:

- Investigation of the efficiency of various 3-D discrete velocity models of LBM for the simulation of turbulent flow past over a bluff body.

- Comparison of two different boundary conditions for benchmark problem of turbulent flow simulation past a square cylinder.

- Implementation of the LBM algorithm on the GPU parallel environment using CUDA programming model.

In this chapter, the first problem is addressed by assessing the comparison of the discrete velocity models (D_3Q_{15}, D_3Q_{19}, and D_3Q_{27}) of the LBM for the simulation of turbulent flow over a bluff body. The second study reports the comparison of the modified bounce-back (BB) method and immersed boundary (IB) method for the treatment of no-slip boundary conditions for the same benchmark case of turbulent flow simulation over a bluff body.

The remainder of the chapter is organized as follows: Section 4.1 provides a comprehensive overview of the simulation geometry and the flow conditions used in the present thesis work. The numerical results are presented in Section 4.2. Section 4.3 summarizes and highlighting the key points of the chapter.

4.1 SIMULATION DOMAIN AND FLOW CONDITIONS

In this section, the geometry of the simulation domain and other flow conditions to study the turbulent flow over a bluff body using LBM are illustrated. Figure 4.1 shows the schematic representation of the flow domain. It consists of a square cylinder (diameter, d = 10 mm) confined in a rectangular duct. The cylinder has complete spans in the duct. The flow is described in the Cartesian coordinate system, where the x-axis is the streamwise dimension, the y-axis is the cross-stream dimension, and the z-axis is the spanwise dimension. In this work, the streamwise, cross-stream, and spanwise dimensions are 20d, 5d, and 3d, respectively. The inflow condition has a mean velocity of U_m, with a thin boundary layer (6% of channel height, H). Random fluctuations are added to the mean velocity for inflow turbulence seeding. The random fluctuations are 6%

of U_m in RMS magnitude. The Reynolds number, defined as $Re_d = U_m d/\nu$ (where ν is the physical kinematic viscosity of the working fluid (i.e. water), is 3000 and the blockage ratio d/H is 20%. The cylinder is placed at the center of the duct and a distance of $0.6H$ from the inlet. A similar flow configuration experimentally studied by Nakagawa *et al.* [1999] for the channel flow. Later, Kim *et al.* [2004] numerically studied the particular flow configuration using a finite volume approach based on LES.
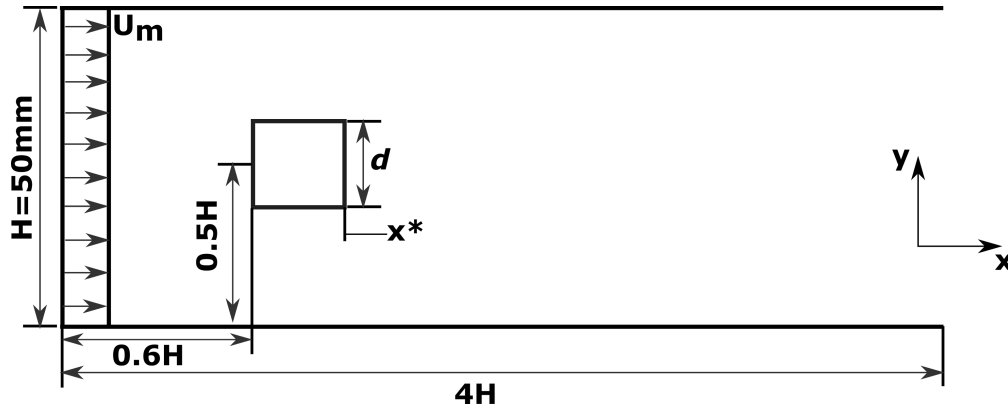

Figure 4.1 : Schematic representation of the flow domain.

In this study, the LES method is used to model the turbulent flow. The Smagorinsky SGS scheme has been used for subgrid-closure with a Smagorinsky constant (C_s) of 0.2 [Koda and Lien, 2015]. The uniform computational grid has $800\times200\times120$ nodes in the streamwise, cross-stream, and spanwise direction, respectively [Koda and Lien, 2015]. Simulations have run for a total of 1 million time-steps, and the turbulent statistics have averaged after every 1000 time-steps. The no-slip boundary conditions have been implemented on the walls of the rectangular duct and cylinder walls using a full way bounce-back rule [Agarwal and Prakash, 2018]. For the inlet, "on-site" velocity boundary conditions have been used, and at the outlet, constant pressure is applied [Agarwal, 2020; Hecht and Harting, 2010; Zou and He, 1997]. A detailed explanation for the boundary conditions is presented in Section 3.2.

4.2 RESULTS AND DISCUSSION
4.2.1 Effect of Discrete Velocity Models of LBM
In this subsection, the results of the effect of 3-D discrete velocity models of LBM (D_3Q_{15}, D_3Q_{19}, and D_3Q_{27}) on the turbulent flow over a bluff body are discussed. The details about the models are presented in Section 3.1. Figure 4.2 shows the instantaneous streamwise velocity component at a spanwise cross-section for all the discrete velocity models used in this study. The formation of vortices at the downstream face of the cylinder and the location of turbulent wakes can be visualized. The visualization plot shows that the diffusion of eddies reduces the turbulent intensity of wakes away from the downstream face of the cylinder. Here as we move away from the downstream face of the cylinder, small-scale eddies inside the turbulent wake start to diffuse in large-scale eddies and results in the growth of larger lumps of wakes with less intensity.

Figure 4.3 presents the profile of time-and spanwise-averaged streamwise velocity along the centerline (z=0) from the downstream face of the cylinder for the D_3Q_{15}, D_3Q_{19}, and D_3Q_{27} discrete velocity models of LBM (represented by red, green and blue markers respectively). The notation $<\cdot>$ denotes time-and spanwise-averaging. The obtained results are compared with the experimental results conducted by Nakagawa *et al.* [1999] and FVM-based numerical simulation
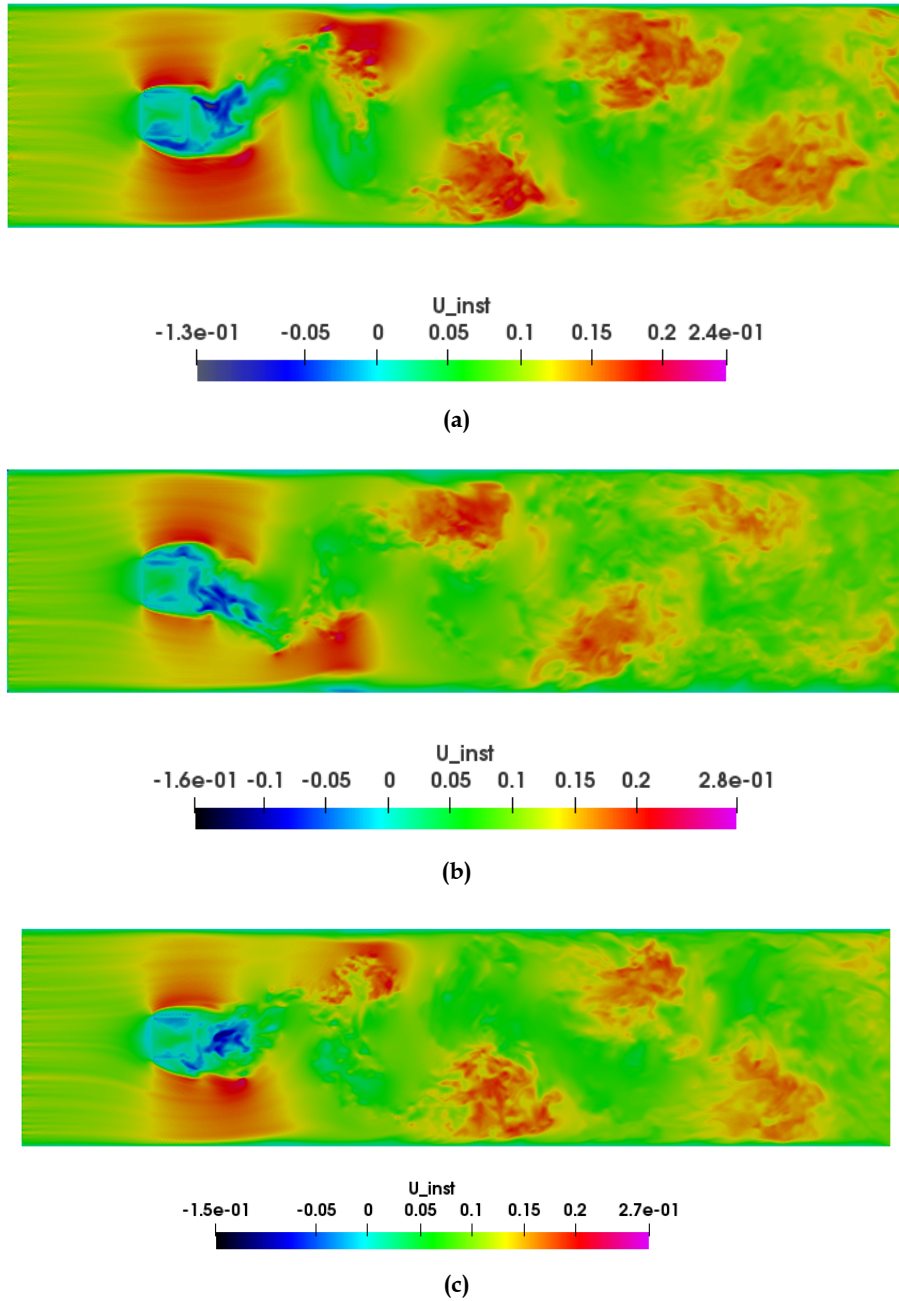
Figure 4.2 : Flow behavior of instantaneous streamwise velocity for (a) D_3Q_{15}, (b) D_3Q_{19}, and (c) D_3Q_{27} velocity models.

results of Kim *et al.* [2004]. All numerical procedures shown in this study are showing a similar pattern except for minor differences in the numerical value. The results show the asymptotic behavior for all studies on all downstream locations beyond $x^*/d \approx 2.4$ (where x^* is the streamwise distance from the downstream face of the cylinder) because no vortices have been identified. In contrast, some deviations have been observed before this downstream location, which is more prevalent up to $x^*/d \approx 0.8$ due to the presence of strong vortices in this region, as shown in Figure 4.2. The deviation in the present study and experiment has been expected because of the boundary condition assumption applied in other studies. The present study assumes the finite depth of the duct, whereas, in other studies, it is assumed to be an infinite channel that affects the velocity
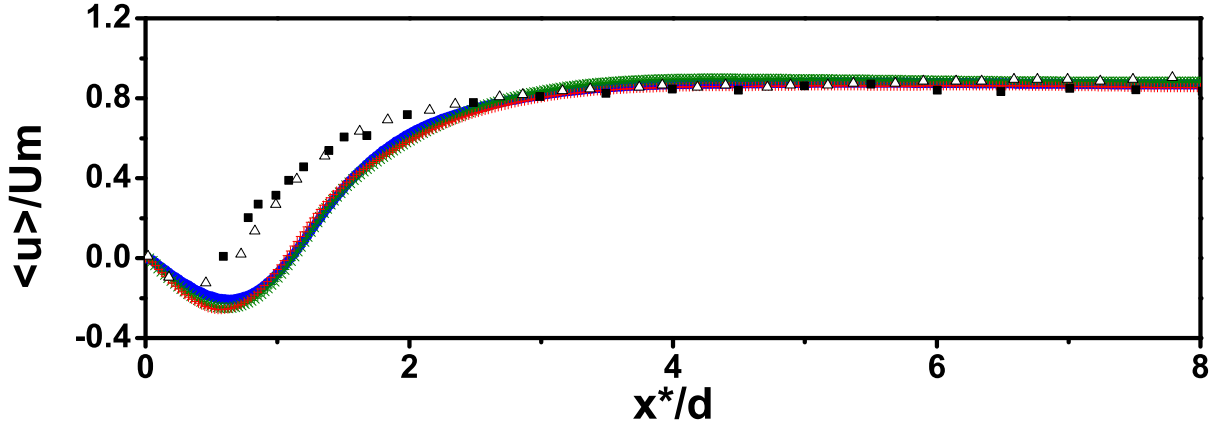
Figure 4.3 : Centerline distribution of mean streamwise velocity (red plus : D_3Q_{15}, green asterisk : D_3Q_{19}, blue open circle : D_3Q_{27}, open triangle : Kim *et al.* [2004], filled square: Nakagawa *et al.* [1999]).

profile and intensity of the vortices. Finite duct assumption would lead to a lower velocity at the spanwise faces of the duct with a no-slip boundary condition leading to a higher velocity at the center location for fixed Re_d = 3000. Moreover, finer grid resolution near the downstream face of the cylinder may result in more accurate agreement with data available in the literature [Nakagawa *et al.*, 1999; Kim *et al.*, 2004]. While comparing present results with them, we found that near the downstream face of the cylinder the agreement between LBM results and experimental data is significantly large. This may be due to the impact of cylinder edge on the flow field, resulting in an increase in velocity just before upstream in the experimental observations. This phenomenon is ignored in the present simulation, and it has been assumed to have a smooth transition from inlet to upstream face and up to past the cylinder [Agarwal, 2020].

Figure 4.4 presents the profiles of mean streamwise velocity at the different streamwise locations. The results are drawn for half of the y-axis (i.e., from $y = 0$ to $y = H/2$) due to symmetry in the y-axis. In Figure 4.4(a), the results show the lower velocity close to $y = 0$ for the present study. This is due to the high-intensity vortices, which can be seen at that location, as evident in Figure 4.2. Furthermore, its negative velocity leads to a decrease in the calculation of mean streamwise
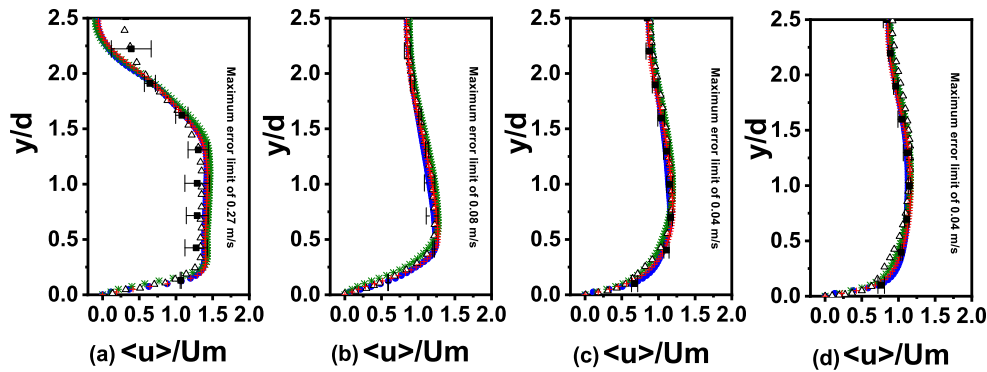

Figure 4.4 : Profiles of mean streamwise velocity (red plus : D_3Q_{15}, green asterisk : D_3Q_{19}, blue open circle : D_3Q_{27}, open triangle : Kim *et al.* [2004], filled square: Nakagawa *et al.* [1999]) : (a) x^*/d = 1.0, (b) x^*/d = 3.5, (c) x^*/d = 6.0, (d) x^*/d = 8.5.

velocity. However, the momentum far away from the location ($y = 0$) for fixed Reynolds number, Re, increased to counter the momentum at a location near to ($y = 0$), which gives rise to the intense vortices just behind the downstream face of the cylinder. Moreover, the lower mean streamwise velocity has been observed near the center ($y = H/2$) to counter the intense vortices again. The results for other figures away from the downstream face of the cylinder, the effect of the vortices diminishes, and all studies give the same results as expected.
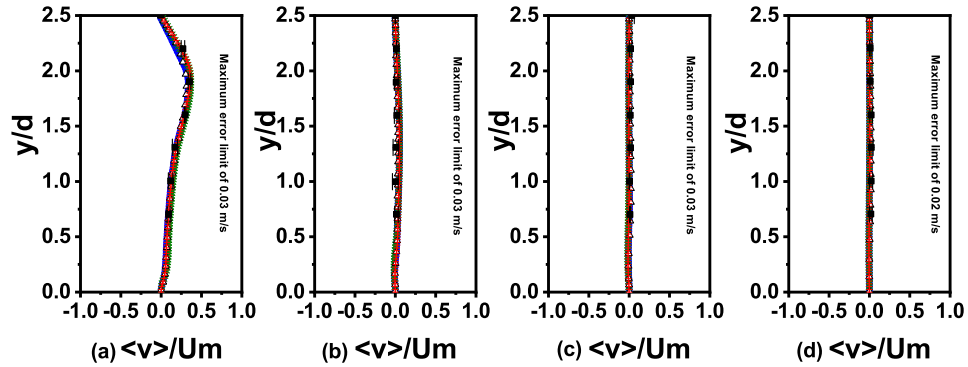

Figure 4.5 : Profiles of mean normal velocity (red plus : D_3Q_{15}, green asterisk : D_3Q_{19}, blue open circle : D_3Q_{27}, open triangle : Kim *et al.* [2004], filled square: Nakagawa *et al.* [1999]) : (a) x^*/d = 1.0, (b) x^*/d = 3.5, (c) x^*/d = 6.0, (d) x^*/d = 8.5.

Figure 4.5 shows the profile of mean normal velocity. The results show that far from downstream cylinder face, small scale eddies are diffused into large scale eddies, it becomes easy for any numerical schemes to capture moment accurately, as evident in Figure 4.5(d). The moment in the perpendicular direction to the flow should follow the net-zero moment transfer for which all studies agree far away from the cylinder, but just after the downstream face of the cylinder, the deviation on moment transfer is plotted in Figure 4.5(a). And, it has been found that the D_3Q_{27} velocity model gives slightly better results in the high turbulent region just after the downstream face of the cylinder.
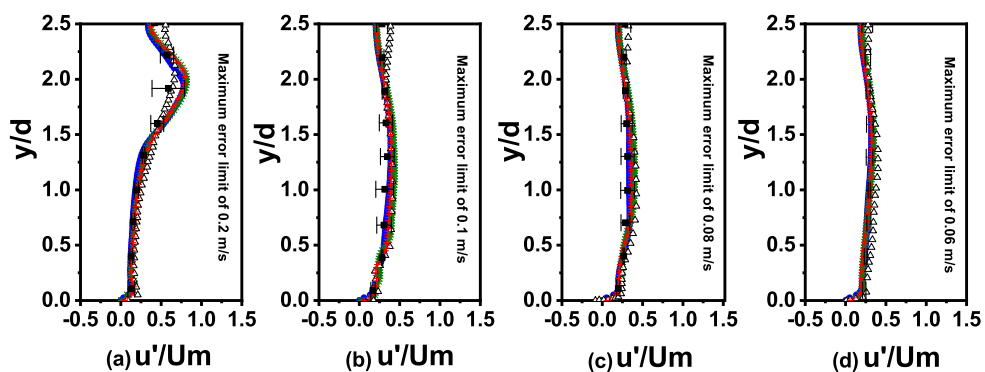

Figure 4.6 : Profiles of RMS streamwise velocity fluctuations (red plus : D_3Q_{15}, green asterisk : D_3Q_{19}, blue open circle : D_3Q_{27}, open triangle : Kim *et al.* [2004], filled square: Nakagawa *et al.* [1999]) : (a) x^*/d = 1.0, (b) x^*/d = 3.5, (c) x^*/d = 6.0, (d) x^*/d = 8.5.

Similar observations have been made for RMS streamwise velocity fluctuations and normal velocity fluctuations, as shown in Figures 4.6 and 4.7. D_3Q_{27}, velocity model, shows the less
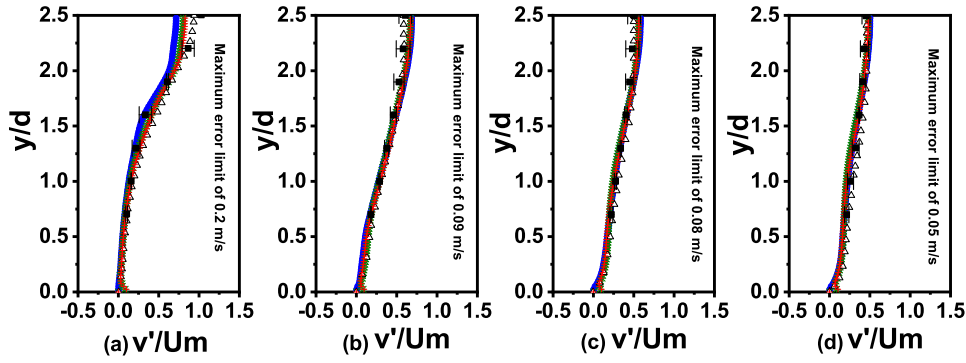
Figure 4.7 : Profiles of RMS normal velocity fluctuations (red plus : D_3Q_{15}, green asterisk : D_3Q_{19}, blue open circle : D_3Q_{27}, open triangle : Kim *et al.* [2004], filled square: Nakagawa *et al.* [1999]) : (a) x^*/d = 1.0, (b) x^*/d = 3.5, (c) x^*/d = 6.0, (d) x^*/d = 8.5..

Figure 4.8 : Profiles of Reynolds shear stress (red plus : D_3Q_{15}, green asterisk : D_3Q_{19}, blue open circle : D_3Q_{27}, open triangle : Kim *et al.* [2004], filled square: Nakagawa *et al.* [1999]) : (a) x^*/d = 1.0, (b) x^*/d = 3.5, (c) x^*/d = 6.0, (d) x^*/d = 8.5.
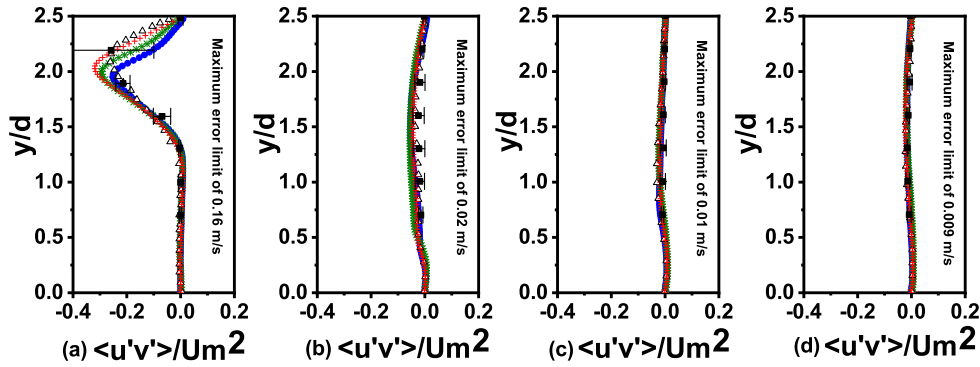
randomness in velocity values for the perpendicular direction of flow near the downstream face of the cylinder compared to other discrete velocity models (i.e., D_3Q_{15} and D_3Q_{19}); however, the results predicted similar flow pattern away from the downstream face of the cylinder for all the discrete velocity models. Reynolds shear stress, which is responsible for drag force on a body, is plotted in Figure 4.8. All schemes predict similar observations far from the flow field with deviations among them near the downstream face of the cylinder. Stress has expected to be highest at the lower edge of the cylinder for an inviscid flow, which is perfectly captured by the present study for the D_3Q_{27} velocity model. Also, it is already mentioned above that the high-intensity vortices have been observed at the center location near the downstream face of the cylinder resulting in the high gradient in velocity vector, which further gives a considerable large shear stress value at that location. Earlier studies by Nakagawa *et al.* [1999] and Kim *et al.* [2004] show a lag in capturing the stress, but overall stress distribution is consistent with the D_3Q_{27} scheme, whereas other velocity models in the present study give over prediction of shear stress distribution. The more isotropic nature of the D_3Q_{27} scheme leads to the stress distribution similar to earlier studies.

Results for drag coefficient derived from shear stress are tabulated in Table 4.1. Results show good agreement between the present study for D_3Q_{27} velocity model and studies performed by Kim *et al.* [2004] for the calculation of drag force in the presence of turbulent flow past a bluff body (here referred to as a square cylinder).

Table 4.1 : Comparison of drag coefficient

Boundary Conditions	Grid Dimension	$\bar{C}_D$
D_3Q_{15}	800×200×120	2.4893
D_3Q_{19}	800×200×120	2.5216
D_3Q_{27}	800×200×120	2.7508
Kim *et al.* [2004]	-	2.76

The present study shows that the LBM method can be implemented fairly to predict turbulent flow in a closed system of fluid flow for a bluff body as an obstruction. LBM is quite able to capture small-scale flow phenomena and large-scale eddies in a turbulent flow. The method can adequately identify the region of vortices and turbulent wake with its intensity. Since the LBM scheme can be effectively implemented for a highly parallelized computing environment due to its local collision operations, the code used in this study has been evaluated for its performance on GPU accelerated parallel environment for all the discrete velocity models and results are presented in Table 4.2. The computational time taken by all the discrete velocity models (D_3Q_{15}, D_3Q_{19}, D_3Q_{27}) concerning the number of threads per block on the GPU cluster has been presented. As the maximum number of threads per block for NVIDIA Tesla P100 is 1024, simulations were performed by varying the number of threads per block (i.e., 1, 8, 64, and 512). The results were collected after 1000 time steps. The MLUPS has been calculated for a varying number of threads per block to measure the performance for all the discrete velocity models. The MLUPS can be calculated with expression given as:

$$MLUPS = \frac{n_x \times n_y \times n_z \times no.\ of\ iterations}{10^6 \times t_r} \tag{4.1}$$

where, n_x, n_y and n_z are the domain sizes in x, y, and z-dimension and t_r is the simulation run time.

The results for the computational efficiency of the discrete velocity models can also be observed in Figure 4.9. As shown in Figure 4.9, the difference between MLUPS values for all the discrete velocity models with a single thread per block is less compared to multiple threads in a block. The result shows that with an increasing number of threads per block, the difference between the MLUPS value among the discrete velocity models increases. Also, one can easily visualize from the plot that increasing the number of velocities deteriorates the computational performance as expected.

4.2.2 Effect of Boundary Conditions

Here, the effect of the modified BB method and IB method for the treatments of the no-slip boundary condition is presented. A particular explicit diffuse direct-forcing immersed boundary-lattice Boltzmann method (IB-LBM) is adopted for the present work. The details and formulation for the BB and IB method are presented in Section 3.2. In this work, the cheap-clipped fourth-order polynomial function proposed by Deen *et al.* [2004] as discussed in Section 3.2.2 is used to mapped unforced velocities at the Eulerian grid nodes on boundary nodes and for distribution of boundary forces on the Eulerian nodes.

Table 4.2 : Computational efficiency of discrete velocity models on GPU cluster

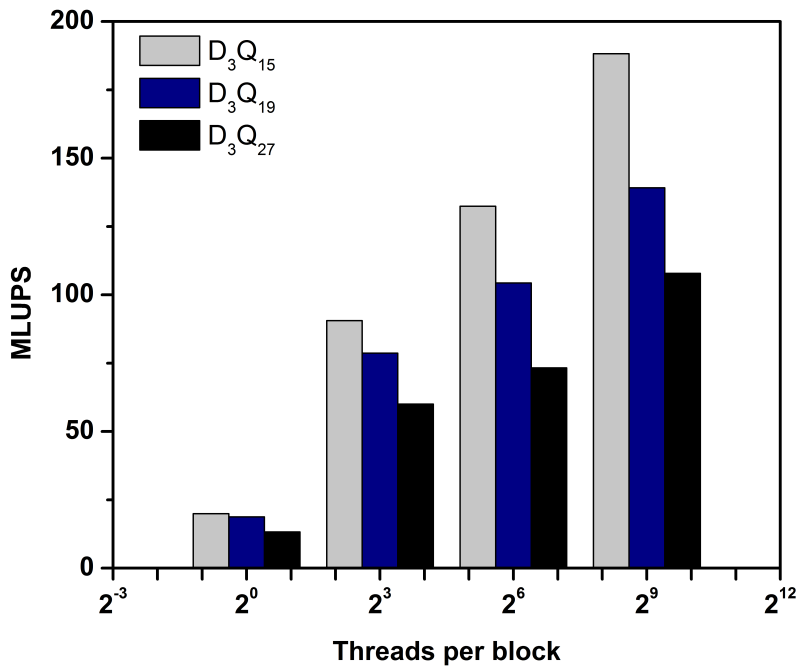| Velocity Model	Threads per block	Computation time (s)	MLUPS
D_3Q_{15}	1	964	19.92
	8	212	90.57
	64	145	132.41
	512	102	188.23
D_3Q_{19}	1	1025	18.73
	8	244	78.69
	64	184	104.35
	512	138	139.13
D_3Q_{27}	1	1452	13.22
	8	320	60.00
	64	262	73.28
	512	178	107.86

Figure 4.9 : GPU performance of discrete velocity.

Figure 4.10 presents the profile of streamwise velocity along the centerline (z = 0) from the downstream face of the cylinder. The results obtained from BB and IB are in fair agreement with the experimental measurement of Nakagawa *et al.* [1999], and LES results of Kim *et al.* [2004]. However, it can be seen that near the downstream face of the cylinder, results show a slight divergence from the experimental and numerical results [Nakagawa *et al.*, 1999; Kim *et al.*, 2004].
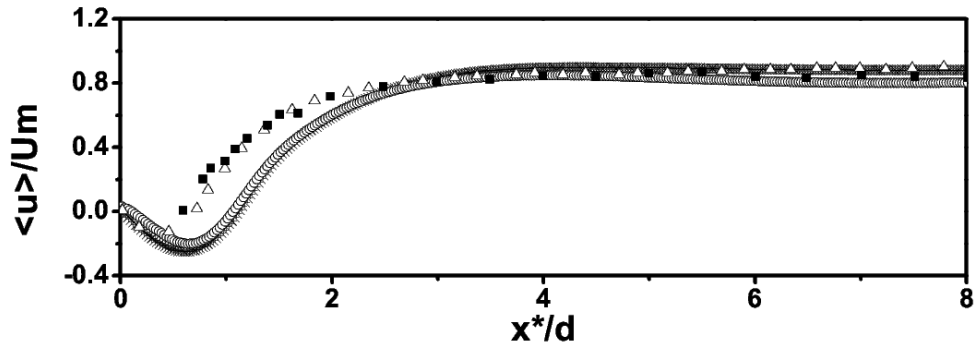
Figure 4.10 : Centerline distribution of mean streamwise velocity (asterisk : BB, open circle : IB, open triangle : Kim *et al.* [2004], filled square : Nakagawa *et al.* [1999]).
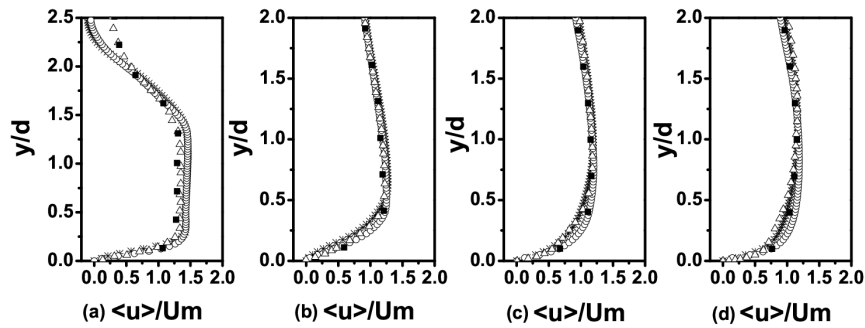

Figure 4.11 : Profiles of mean streamwise velocity (asterisk : BB, open circle : IB, open triangle : Kim *et al.* [2004], filled square : Nakagawa *et al.* [1999]) : (a) x^*/d = 1.0, (b) x^*/d = 3.5, (c) x^*/d = 6.0, (d) x^*/d = 8.5.
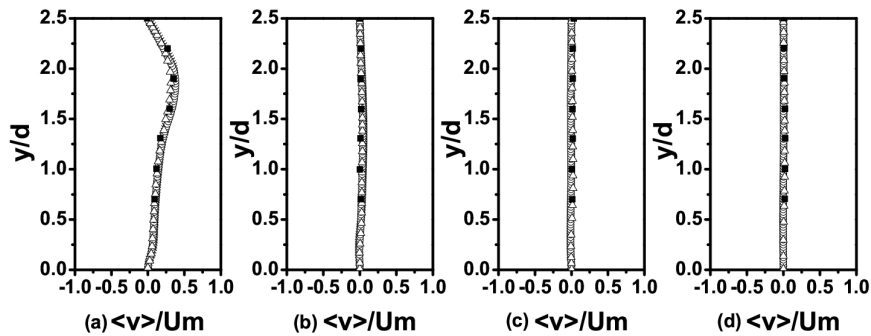

Figure 4.12 : Profiles of mean normal velocity (asterisk : BB, open circle : IB, open triangle : Kim *et al.* [2004], filled square : Nakagawa *et al.* [1999]) : (a) x^*/d = 1.0, (b) x^*/d = 3.5, (c) x^*/d = 6.0, (d) x^*/d = 8.5.

Profiles of time-and spanwise-averaged mean velocities, turbulent fluctuations, and Reynolds shear stress are shown in Figures 4.11-4.15, respectively, for different streamwise location (x*/d = 1.0, 3.5. 6.0, 8.5). In Figure 4.11(a), a similar deviation has been observed in the mean streamwise velocity near the downstream face of the cylinder for both BB and IB methods. The

other figures show excellent agreement with the literature [Nakagawa *et al.*, 1999; Kim *et al.*, 2004] away from the cylinder face. The results for mean normal velocity shown in Figure 4.11 presents a good match for both BB and IB methods with experimental measurements and LES results. Moreover, it can be seen from Figures 4.11 and 4.12 for both BB and IB methods that the mean streamwise velocity is much affected by the pair of vortices formed behind the cylinder compared to mean normal velocity.
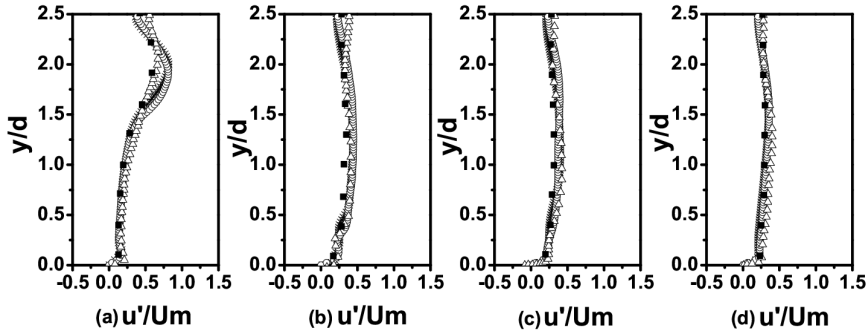
Figure 4.13 : Profiles of RMS streamwise velocity fluctuations (asterisk : BB, open circle : IB, open triangle : Kim *et al.* [2004], filled square : Nakagawa *et al.* [1999]) : (a) x^*/d = 1.0, (b) x^*/d = 3.5, (c) x^*/d = 6.0, (d) x^*/d = 8.5.
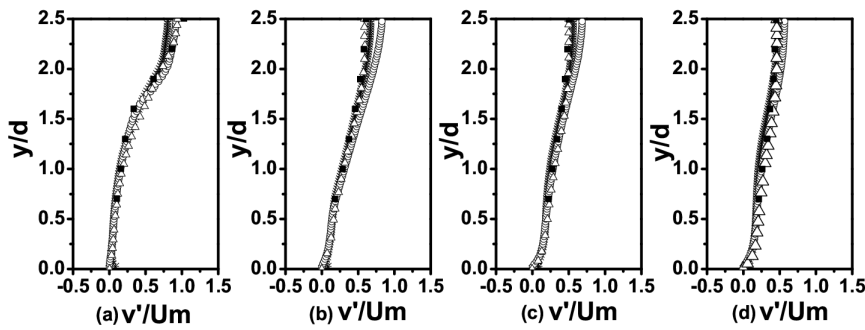
Figure 4.14 : Profiles of RMS normal velocity fluctuations (asterisk : BB, open circle : IB, open triangle : Kim *et al.* [2004], filled square : Nakagawa *et al.* [1999]) : (a) x^*/d = 1.0, (b) x^*/d = 3.5, (c) x^*/d = 6.0, (d) x^*/d = 8.5.
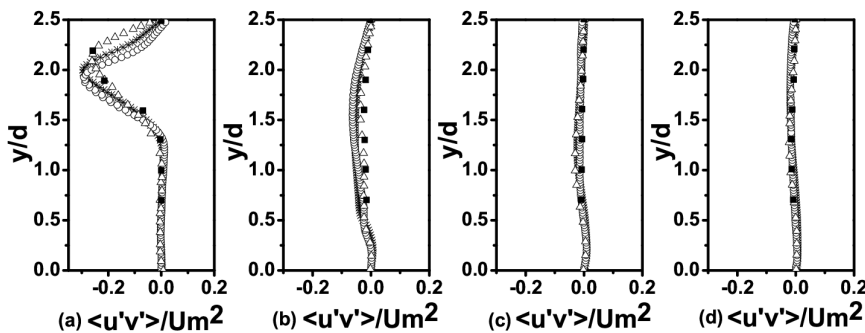
Figure 4.15 : Profiles of Reynolds shear stress (asterisk : BB, open circle : IB, open triangle : Kim *et al.* [2004], filled square : Nakagawa *et al.* [1999]) : (a) x^*/d = 1.0, (b) x^*/d = 3.5, (c) x^*/d = 6.0, (d) x^*/d = 8.5.

For the case of turbulent fluctuations, as shown in Figures 4.13 and 4.14, disagreement also

continues in the RMS streamwise velocity fluctuations near the downstream face of the cylinder are quickly recovered in the downstream direction away from the cylinder for both BB and IB method. Figure 4.15 shows profiles of Reynolds shear stress at a different streamwise location, and similar variation is observed with both BB and IB methods near the downstream face of cylinder compared to Nakagawa *et al.* [1999] and Kim *et al.* [2004] results. The results on other streamwise locations displayed excellent correspondence with literature data Nakagawa *et al.* [1999]; Kim *et al.* [2004].

The comparison of mean drag coefficient $\bar{C}_D$ is shown in Table 4.3. The table shows good agreement of the mean drag coefficient obtained from the BB method with the LES results of Kim *et al.* [2004]. However, a slightly higher value in the simulation of Kim *et al.* [2004] can be because of capturing the resistance of the flow field by the edge of the cylinder surface, which is absent in our study. The IB method over-predicted the mean drag coefficient. Further, the comparison of the BB and IB method based on computational efficiency is shown in Table 4.4. The computational time taken by both approaches concerning the number of threads per block on the GPU cluster is presented. The performance is measured from the MLUPS, and expression is given in Eqn. (4.1).
As seen in Table 4.4., the MLUPS numbers for the BB method are 65.01, 89.95, and 163.57, whereas

Table 4.3 : Comparison of drag coefficient

Boundary Conditions	Grid Dimension	$\bar{C}_D$
BB	$800{\times}200{\times}120$	2.52
IB	$800{\times}200{\times}120$	2.96
Kim *et al.* [2004]	-	2.76

Table 4.4 : Computational efficiency of BB and IB method on GPU cluster

Velocity Model	Threads per block	Computation time (s)	MLUPS
BB	8	295.34	65.01
	64	213.44	89.95
	512	117.37	163.57
IB	8	431.96	44.45
	64	327.79	58.57
	512	208.87	91.92

MLUPS numbers for the IB method are 44.45, 58.57, and 91.92 for 8, 64, and 512 threads per block, respectively. It shows that the computationally BB approach is faster than the IB method. It can also be observed from Table 4.4 that there is a difference of approx 32% in MLUPS of BB and IB method for 8 number of threads per block. This difference increases with the increasing number of threads per block (i.e., approx 34% for 64 number of threads per block and approx 44% for 512 number of threads per block). It summarizes that the difference in the computational performance of BB and IB on the GPU cluster is small for a lesser number of threads per block, while the increasing number of threads per block deteriorates the performance of the IB method compared to the BB method. For enhancing the computational performance of the IB method, the continuous transfer of variables from the host (i.e., CPU) to the device (i.e., GPU) and vice-versa must be avoided. This continuous transfer of data from the host to device and vice-versa is because the velocity components of surrounding fluid nodes across the boundary nodes are transferred from the device (i.e., GPU) to the host in order to calculate the forces at the boundary nodes on the host (i.e., CPU) architecture, and these forces then again transferred to the device for further simulation.

4.3 SUMMARY

In this chapter, the simulation of turbulent flow over a bluff body using LBM is presented. The chapter comprises the results of two studies. The first study reported the effect of 3D discrete velocity sets (i.e., D_3Q_{15}, D_3Q_{19}, and D_3Q_{27}) of LBM on the flow behavior of turbulent flow over a bluff body. However, the impact of the different boundary conditions (i.e., BB and IB) is explored in the second study. The simulations have been carried out for benchmark case of flow past a square cylinder confined in a rectangular duct at Re_d = 3000 for both the studies. LES approach has been used to simulate turbulent flow. The Smagorinsky SGS model is used to resolve the small-scale turbulent structures. The obtained simulation results for both studies are validated through the experimental and numerical results available in the literature. Moreover, a parallel computer code has been developed using CUDA programming model to run on a multicore GPU platform, and the computational performance has also been presented. For the first study, results are presented for the comparative assessment of 3D discrete velocity sets (i.e., D_3Q_{15}, D_3Q_{19}, and D_3Q_{27}) of LBM based on the accuracy and performance of the code in the GPU parallelized environment. The results obtained from LBM-LES are stable and in good agreement with the experimental data. Furthermore, results showed that the LBM method effectively captures the small-scale phenomenon and large-scale fluid properties. The obtained results depicted better accuracy for the D_3Q_{27} velocity model over other discrete velocity models at the cost of computation time. Parallelization of code reduces the computational cost drastically as more threads are available for computation. Computation time for the D_3Q_{27} velocity model has found almost 1.5 times the computation time of the D_3Q_{15} velocity model, and the ratio for computation times for both schemes widens more as the number of threads increases. The study suggests that the LBM can capture the turbulent flow even in the region of high Reynolds shear stress. The study provides insight for selecting the suitable LBM discrete velocity scheme based on the accuracy required and computational power needed, mainly for the simulation of benchmark problems of fluid flow such as flow past a single obstacle. In another study, the simulaions are performed to visualize the effect of boundary conditions on the flow behavior. The BB and IB method are taken into consideration for the simulation. The results obtained from both the boundary method are in nearly similar agreement with the experimental and numerical results obtained by other researchers in the past studies. However, from a computational perspective, the obtained results show that the bounce-back approach is computationally more efficient than the immersed boundary method. The above studies are intended to be expanded to simulate complex fluid dynamics problems on large domains, which will involve turbulent flow and fluid-structure interaction, and require high computational performance. The same are discussed in the subsequent chapter.

…